nature communications

Article

https://doi.org/10.1038/s41467-025-66963-7

Recyclable quasi-solid-state dynamic windows via reversible dual-metal electrodeposition for building energy modulation

Received: 28 March 2025

Accepted: 18 November 2025

Published online: 01 December 2025

Check for updates

Bing Xu[1], Wenting Wu[2], Yingxin Zhang[1], Chenglong Qiu[1], Yue Zhu[1], Jingyi Wu[1], Weiqian Tian[1], Minghua Huang[1], Huanlei Wang[1,3] ✉, Pooi See Lee[2] ✉ & Jingwei Chen[1,3] ✉

Reversible metal electrodeposition-based electrochromic devices (RMEDs) with broadband regulation manifest great promises as smart windows to increase building energy efficiency. However, manufacturing durable and scalable RMEDs at an agreeable cost is still challenged by the limited reversibility of interfacial plating (tinting)/stripping (bleaching). Here, we report a quasi-solid-state hydrogel electrolyte with well-tuned Cu:Zn ratio and pH values to achieve highly reversible CuZn-RMEDs. The dual-metal CuZn electrolyte ensures staged nucleation and homogeneous CuZn growth, and the appropriate pH guarantees effective stripping of CuZn metal layers, thus attaining reduced metal deposition activation energy (6.7 kJ mol^{-1}), increased coloration efficiency, large transmittance modulation (ΔT = 78% @550 nm), and excellent reversibility (ΔT retention over 90% after 3000 cycles). In addition, the quasi-solid-state hydrogel matrix with abundant molecular chains can inhibit strong hydrogen bonds in aqueous electrolyte, achieving anti-freezing (−20°C) and leakage-free CuZn-RMEDs with fast switching kinetics (coloration time t_c = 15.0 s, bleaching time t_b = 24.0 s), extended memory effect, efficient thermal insulation, and effective reusability (2000 cycles) of both the transparent conductor and hydrogel electrolyte. The as-assembled CuZn-RMEDs manifest 18% to 33% energy saving across different climatic regions. This quasi-solid-state CuZn-RMED is a successful embodiment of cost-effective and durable electrochromic smart windows towards increasing buildings' energy efficiency.

Buildings are responsible for about 40% of the total energy consumption in modern society, and windows, as the key interface for light and heat exchange, are the least energy-efficient components in buildings[1–4]. Statistically, smart windows that dynamically regulate light and heat transfer can save about 10% of lighting and air conditioning energy consumption[5–9]. Among available smart windows, electrochromic smart windows (ESWs) are more favorable than thermochromic and photochromic smart windows in terms of optical

[1]School of Materials Science and Engineering, Ocean University of China, Qingdao, China. [2]School of Materials Science and Engineering, Nanyang Technological University, Singapore, Singapore. [3]Qingdao Key Laboratory of Marine Extreme Environment Materials, Ocean University of China, Qingdao, China. ✉e-mail: huanleiwang@ouc.edu.cn; pslee@ntu.edu.sg; chenjingwei@ouc.edu.cn

modulation range, response time, and on-demand control[10–12]. ESWs reversibly modulate optical properties (transmittance *T*%, absorbance, and reflectance) in response to an applied electrical pulse (current or voltage)[13,14]. Currently, the mainstream ESWs rely on reversible ion embedding/de-embedding, achieving visible (VIS) or visible/near-infrared (NIR) dual-band regulation[15–18]. Nevertheless, they fall short of color neutrality, privacy states, and require pre-deposited EC layers[19–21]. Comparatively, reversible metal electrodeposition-based devices (RMEDs) switch between transparent and deeply tinted states via metal deposition/stripping, offering simpler configuration, near color neutrality, and broadband regulation (Fig. 1a)[16,22,23]. The high extinction coefficients of metals enable RMEDs to reach privacy states ($T\% < 0.1\%$) across the solar spectrum (300–2500 nm) with only tens of nanometers of plating[24,25]. Additionally, RMEDs can also offer tunable IR emissivity for radiative cooling, and colored states via plasmonic resonance (e.g., Ag, Au, Cu)[26,27].

However, manufacturing durable and scalable RMEDs is still challenged by the cost disadvantages of Au/Ag[28–30], corrosion of transparent electrodes by Cu/Bi[31–34], low reversibility of Ni/Sn[35–37], and dendrites and side reactions of Zn[38–40]. Although introducing heterogeneous metal (e.g., Cu/Zn[5], Cu/Bi[34]) has shown potential in regulating nucleation/growth kinetics, response speed, and cycle stability, the more fundamental challenge lies in the inherent defects of liquid electrolytes. Organic electrolytes exhibit biotoxicity, flammability, and volatility[41,42], while aqueous electrolytes are constrained by narrow electrochemical windows and low environmental adaptability[43–45]. Additionally, the inherent swelling and leakage risks of liquid electrolytes severely limit the scalability and service life of RMEDs. Therefore, a leakage-free (quasi-) solid-state electrolyte with fast kinetics, chemical/electrochemical stability, biosafety, and environmental friendliness is needed in practical RMEDs.

Hydrogel electrolytes—preferred in ECD applications due to their safety, biocompatibility, mechanical flexibility, and high transparency—contain abundant hydrophilic functional groups along their polymer chains. These functional groups promote the migration of ions within the polymer network, ensuring uniform ionic flux for ECD operation[46–48]. Given this, we engineered a hydrogel electrolyte composed of Cu/Zn dual-metal salts and hydrophilic polyacrylamide (PAM) networks (Fig. 1b). The dual-metal CuZn hydrogel electrolyte is envisioned to enable staged nucleation and uniform growth, ensuring

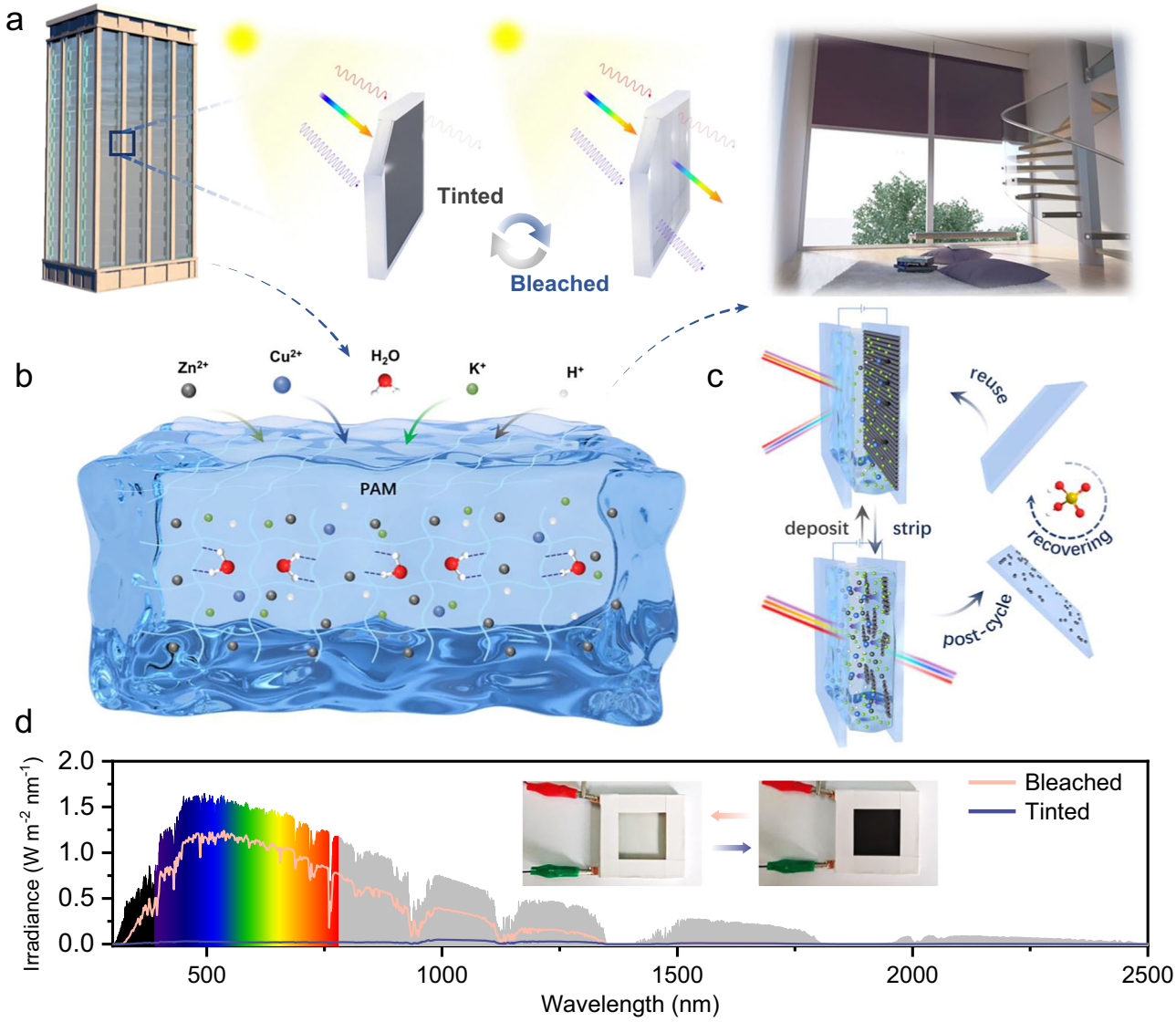

Fig. 1 | Schematic illustration of hydrogel-based reversible CuZn metal electrodeposition devices for smart window applications. a Schematic diagram of the optical modulation offered by CuZn reversible metal electrodeposition-based electrochromic devices (CuZn-RMEDs). **b** Dual-metal CuZn hydrogel electrolyte. **c** The working mechanism of CuZn-RMEDs and the F-doped SnO_2 (FTO) recycling process. **d** Solar irradiance of CuZn-RMEDs in tinted and bleached states in the wavelength range from 300 to 2500 nm under AM1.5 G, insets are the photographs of bleached and tinted CuZn-RMEDs.

rapid and reversible CuZn electroplating/stripping (Fig. 1c) and achieving a dark state across the solar spectrum (Fig. 1d) in leakage-free quasi-solid-state CuZn-RMEDs.

In this work, the dual-metal electrolyte allows uniform CuZn deposition, improved transmittance modulation (ΔT = 78% @550 nm), and significantly enhanced cycle life (ΔT retention over 90% after 3000 cycles). Further incorporation of PAM matrix renders CuZn-PAM hydrogel electrolyte with excellent environmental stability, while maintaining superior ionic conductivity (11.3 mS cm^{-1}). The extensive interactions between hydrophilic PAM chains and polar H_2O molecules can effectively suppress hydrogen evolution reactions (HER)[46,49] and inhibit water freezing at low temperature, while the interfacial compatibility between hydrogel electrolyte and FTO (F-doped SnO_2) glass allows facile assembly of leakage-free RMEDs with extended memory effect. Hence, the as-assembled quasi-solid-state CuZn-RMEDs show accelerated switching kinetics (t_c = 15.0 s, t_b = 24.0 s), large operational temperature range (−20 to 60 °C), good cycling stability, and thermal insulation capability. The energy consumption simulation results indicate that the quasi-solid-state CuZn-RMED is able to reduce energy consumption by 18–33% compared to conventional static windows. Additionally, the CuZn-RMEDs allow the recycling of the transparent conductors and hydrogel electrolytes. The recyclable quasi-solid-state dynamic windows with excellent optical modulation capability, durability, cost-effectiveness, and high energy efficiency, demonstrated in this work, offer feasible solutions towards decarbonized and even net-zero buildings.

Results

Optimization of aqueous CuZn-RME electrolytes

In RMEDs, reversible transition between tinted and bleached states is achieved through the deposition and stripping of metals. The quasi-solid-state hydrogel electrolytes for RMEDs were formulated based on dual-metal (Cu^{2+} and Zn^{2+}) ions. The selection of dual-metal CuZn can be rationalized by the safety, environmental benignity, low cost, and neutral coloration of Zn, while the addition of heterogeneous Cu^{2+} can regulate the nucleation and growth of dual-metal CuZn layers via staged nucleation and induced homogeneous growth, because Cu possesses relatively low oxophilicity, inherent inertness to HER, higher standard electrode potential (E_0 of Cu^{2+}/Cu = 0.34 V vs. standard hydrogen electrode [SHE]) than that of Zn^{2+}/Zn (−0.76 V vs. SHE), and excellent zincophilicity[50].

Prior to the fabrication of CuZn-RMEDs, the modulatory effect of Cu^{2+} on the nucleation and growth behavior of CuZn on FTO glass electrode was first assessed in a series of aqueous CZ electrolytes (denoted as C*x*Z*y*, where *x*: *y* stands for Cu^{2+}/Zn^{2+} ratios, Supplementary Fig. S1). An apparent bluish color was noticed with higher Cu^{2+} concentration. In-situ transmittance variations (@550 nm) of FTO electrodes during cyclic voltammetry (CV) scan (10 mV s^{-1}) in these electrolytes were first recorded (Fig. 2a, Supplementary Fig. S2). During the negative scan, the cathodic current in pure C0Z1 begins to increase near −1.0 V (vs. Ag/AgCl) (Supplementary Fig. S2a), attributed to the reduction of Zn^{2+} to Zn, and the oxidation peak near −0.9 V (vs. Ag/AgCl) during the positive scan corresponds to the oxidation of Zn to Zn^{2+}. However, the limited *T*% variation and the indistinct color change between the tinted and bleached states (as seen in the insets) indicate the limited RME reversibility in C0Z1 electrolyte, making it difficult to form a dense Zn layer. With Cu^{2+} incorporation, extra redox peaks can be observed from the CV curves and larger *T*% variations are recorded (Fig. 2a, Supplementary Fig. S2b–e). The newly appeared cathodic peaks between −0.2 and −0.8 V are presumably ascribed to the sequential reduction of Cu^{2+} to Cu^+ and Cu^+ to Cu, and the extra anodic peaks noticed between −0.4 and 0.2 V are attributed to the oxidation of Cu to Cu^+ and Cu^+ to Cu^{2+}. The distinct color change and prominent *T*% variation between the tinted and bleached states certainly confirm that Cu^{2+} can promote the reversible dual-metal CuZn-RME. Considering the color change, current responses in CV curves and the in-situ *T*% variation, Cu^{2+}/Zn^{2+} ratio is optimized to be 1:5 (C1Z5), ensuring large ΔT and good RME reversibility (Fig. 2a). The optimized Cu^{2+}/Zn^{2+} ratio in aqueous electrolyte slightly deviates from our previous study in dimethyl sulfoxide solvent (1:10)[5], which is likely due to the altered solvation structure and different nucleation energy barriers[51,52]. The transmittance spectra of FTO electrodes at initial, tinted (−1.0 V, 60 s), and bleached (0.8 V, 60 s) states were further recorded in different aqueous electrolytes (Fig. 2b, Supplementary Fig. S3). Predictably, a large ΔT (78% @550 nm) is achieved in C1Z5 (Fig. 2b), outperforming those in other CZ aqueous electrolytes (between 64% and 74%), while almost no ΔT (only 2% @550 nm) is observed in C0Z1 (Supplementary Fig. S3a). Furthermore, the in-situ dynamic *T*% variations (@550 nm) under repeated voltage steps (−1.0 V for 20 s and 0.8 V for 60 s) were also recorded (Fig. 2c, Supplementary Fig. S4). Comparatively, a high ΔT (57%) is maintained in C1Z5 with a fast response kinetics (t_c = 13.7 s, t_b = 5.4 s), demonstrating excellent reversibility with rapid kinetics.

In order to corroborate the superior RME reversibility in C1Z5 aqueous electrolyte, the surface morphology and composition of plated metal layers (−1.0 V, 30 s) were captured by scanning electron microscopy (SEM, Supplementary Figs. S5 and S6), and X-ray diffraction (XRD) patterns (Supplementary Fig. S7), respectively. A uniform layer of metal nanoparticles (thickness ~900 nm) is deposited on the FTO electrode in C1Z5, while sparse and bulky microparticles are obtained in C0Z1 (thickness 200–500 nm). This explains the favorable EC performance achieved in C1Z5 electrolyte, forming a uniform and dense CuZn dual-metal layer with excellent light modulation capability. The optimal performance achieved in C1Z5 electrolyte may be attributed to the fact that a low concentration of Cu^{2+} can only provide a limited number of Cu nuclei and active sites required for Zn^{2+} deposition, which is insufficient to fully achieve reversible dual-metal CuZn plating/stripping, leading to a lower ΔT and slower switching speed. Conversely, excessive Cu^{2+} concentration would lead to a deeper electrolyte color (Supplementary Fig. S1) and inhibit the stripping efficiency, sacrificing the optical contrast (Supplementary Fig. S3) and switching kinetics (Supplementary Fig. S4).

The excellent reversibility and switching kinetics of CuZn-RME on FTO electrodes in C1Z5 electrolyte inspired further evaluation on the cycling stability. Notably, although C1Z5 offers large ΔT and fast switching, it can hardly retain a decent cycling performance, with obvious ΔT degradation (ΔT retention of 52%) after only about 300 cycles (Supplementary Fig. S8a). Such poor cycling stability is certainly far from satisfactory for practical applications, and the decreased ΔT mainly stems from the decreasing *T*% at the bleached state, due to the accumulated undissolved species on the FTO electrode (Supplementary Figs. S9 and S10). SEM and X-ray photoelectron spectroscopy (XPS) characterizations were further used to investigate the morphology and chemical composition of accumulated species on cycled FTO electrodes (1000 cycles). Dispersed micron-sized flaky residues were observed on the FTO surface after cycling in C1Z5 (Supplementary Fig. S11a), consisting of Cu, Zn, and O elements. The Cu2*p* XPS spectra of the residue show multiple Cu2$p_{1/2}$, Cu2$p_{3/2}$, and satellite peaks with broad half-peak widths, while the characteristic peaks corresponding to Cu^+ and Cu^0 near 932 eV have relatively low intensities, indicating that Cu primarily exists as Cu^{2+} (Supplementary Fig. S12a). The broad half-width of Zn2$p_{1/2}$ and Zn2$p_{3/2}$ peaks in the corresponding Zn2*p* XPS spectra also indicates that Zn is primarily present as Zn^{2+}. Therefore, the flaky residues on FTO electrodes cycled in C1Z5 are mainly composed of $CuO/Cu(OH)_2$ and $ZnO/Zn(OH)_2$.

In order to avoid the accumulated deposits during extended cycling, a small amount of H^+ is added into the C1Z5 aqueous electrolyte (Supplementary Fig. S13). For aqueous electrolytes, the pH value also significantly affects the interfacial dynamics, reversibility, and cycling stability of RME[34,53,54]. Selecting an appropriate H^+

https://doi.org/10.1038/s41467-025-66963-7

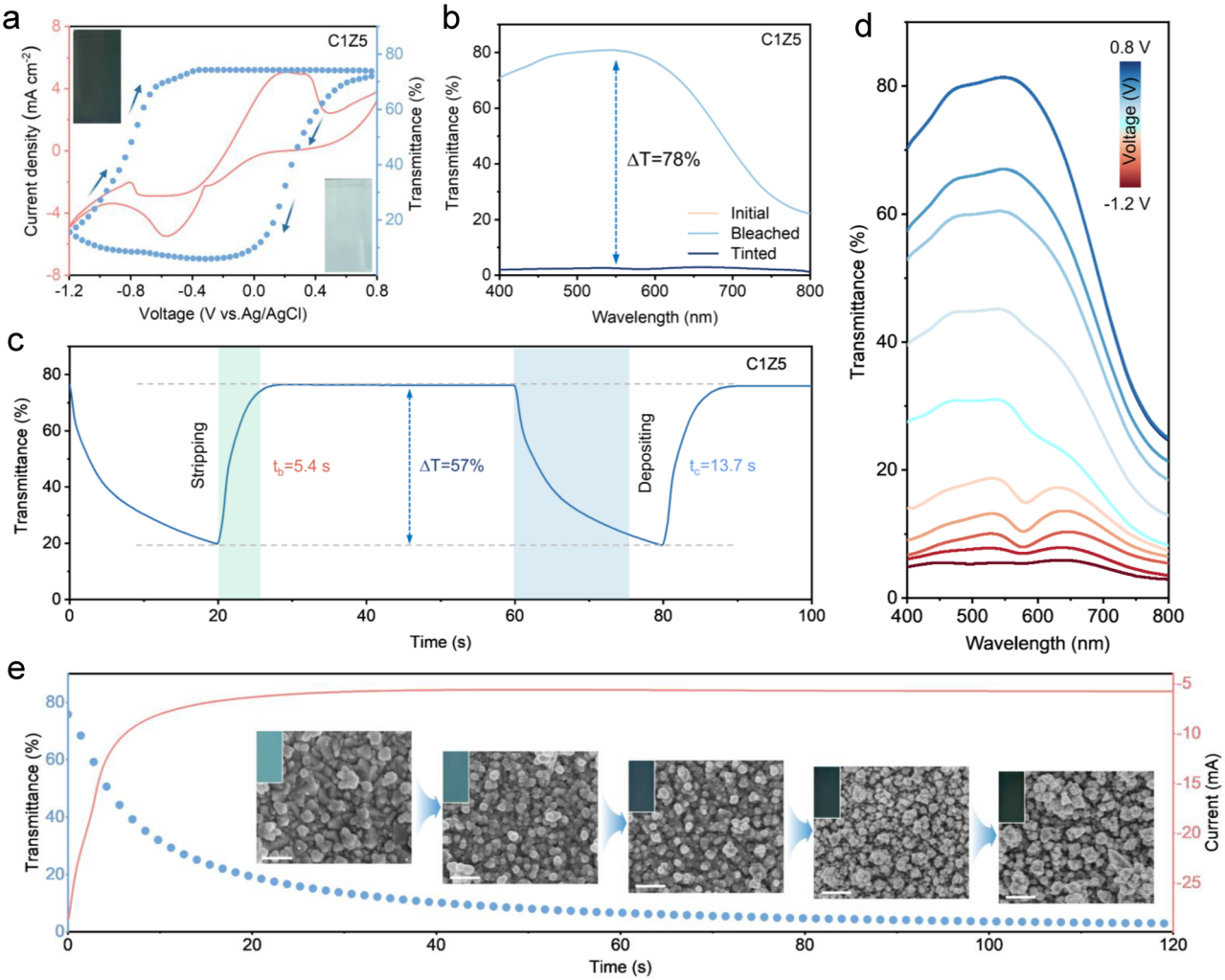

Fig. 2 | Electrochemical and electrochromic performance of reversible metal electrodeposition (RME) on F-doped SnO_2 (FTO) electrodes in aqueous electrolytes. a CV curve of FTO electrode (scan rate of 10 mV s^{-1}) and the in-situ transmittance variation (@550 nm) in C1Z5 (Cu^{2+}/Zn^{2+} ratio of 1:5) electrolyte. Insets are the photographs of FTO electrodes in tinted and bleached states. **b** UV–VIS transmittance spectrum of FTO electrodes in initial, tinted (−1.0 V vs. Ag/AgCl, 60 s) and bleached states (0.8 V, 60 s) and **c** dynamic *T*% (@550 nm) variation under voltage steps (−1.0 and 0.8 V) in C1Z5 electrolyte. **d** Transmittance spectra of FTO electrodes in C1Z5H20 (H^+ concentration of 20 mM) at different potentials (−1.2 to 0.8 V). **e** In situ transmittance and current versus time curves of FTO when plated in C1Z5H20 at −1.2 V and the corresponding SEM images and optical photographs at different times (5, 10, 30, 60, 120 s), scale bar 500 nm.

concentration can accelerate the charge transfer at the FTO electrode/electrolyte interface, suppress the growth of irreversible side products, and extend the cycle life. With increased concentration of H^+, *T*% at bleached states are notably stabilized during repeated cycling (Supplementary Fig. S8b–e), emphasizing the importance of pH regulation in achieving extended CuZn-RMEDs cycling. Likewise, considering the Δ*T*, switching kinetics, and cycling stability, the concentration of H^+ in the C1Z5H aqueous electrolyte was further optimized to 20 mM (Supplementary Figs. S8–S16), and the FTO retains a smooth and flat surface with minimal accumulated deposits after cycling (1000 cycles) in C1Z5H20 (H^+ concentration of 20 mM) electrolyte (Supplementary Fig. S11b). A lower concentration of H^+ may still lead to the accumulation of irreversible side products, resulting in slower response speeds and decreased *T*% in the bleached state, while a higher concentration of H^+ may prolong deposition time and accelerate dissolution of the dual-metal CuZn layer and HER side reactions during plating, resulting in deterioration of cycling performance (Supplementary Fig. S8). Therefore, C1Z5H20 electrolyte was employed for subsequent discussions unless otherwise specified.

With well-tuned aqueous electrolyte formulation, the transmittance spectra of FTO electrodes under different voltages were recorded (Fig. 2d). The FTO electrode exhibits progressively reduced *T* % across the visible wavelength along with decreased plating potential, a low *T*% of <6% (@550 nm) is achieved under a negative bias of −1.2 V, and can be fully bleached to its initial state (*T*% = 81% @550 nm) when positively biased at 0.8 V. The absorption spectra within the same wavelength range (Supplementary Fig. S17) also indicate that CuZn-RME has a highly controllable and reversible optical switching capability. During plating at −1.2 V, the in-situ *T*% (@550 nm) of FTO electrode and the corresponding metal layer morphology were recorded (Fig. 2e). Unlike the formation of randomly distributed bulky microparticles in C0Z1 electrolyte (Supplementary Fig. S5a), plating in C1Z5H20 undergoes uniform nucleation at the initial stage and gradually evolves into spherical nanoparticles, eventually forming a uniform and dense metal film with a severely low transmittance of 3% (120 s). Notably, a low *T*% (6%) is already achieved after only 60 s, demonstrating the fast plating kinetics and excellent light-blocking capability of CuZn-RME in C1Z5H20 aqueous electrolyte.

Aside from morphology, the composition and chemical structure evolution of plated metal layers were also characterized via ex situ grazing incidence X-ray diffraction (GIXRD, Fig. 3a) and XPS tests (Fig. 3b, Supplementary Fig. S18). As depicted in Fig. 3a, a reduction

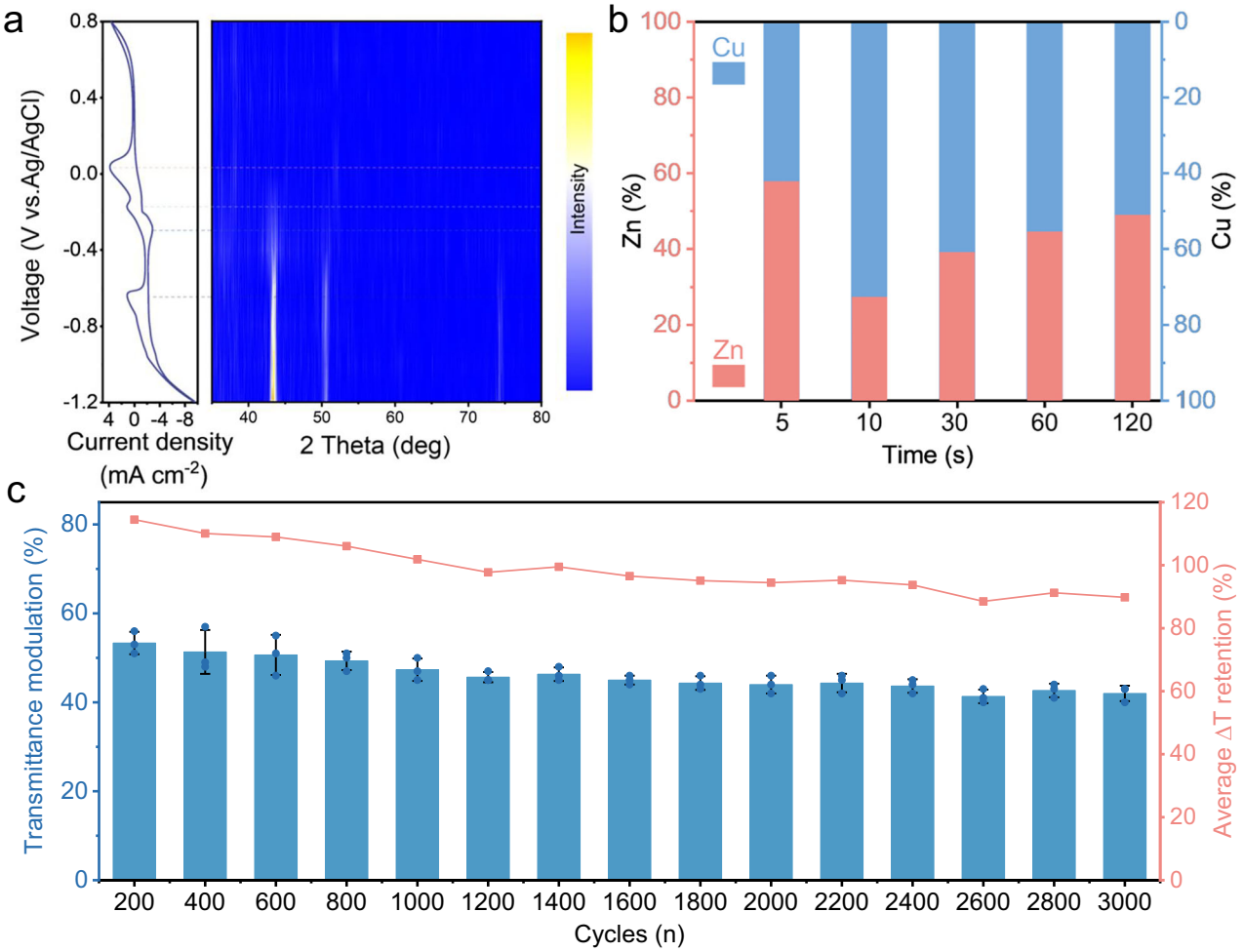

Fig. 3 | Plating and stripping mechanism of CuZn reversible metal electrodeposition (CuZn-RME). a Ex-situ Grazing Incidence X-ray diffraction (GIXRD) of CuZn-RME during CV scans (5 mV s^{-1}). **b** Atomic percentage of Zn and Cu in dual-metal CuZn layers when plated at −1.0 V for 5, 10, 30, 60, and 120 s. **c** Transmittance (@550 nm) variation and average Δ*T* retention of FTO electrode in CuZn-RME under tinted (−1.0 V, 10 s) and bleached (0.8 V, 40 s) states during long-term cycling (3000 cycles). All the error bars represent the standard deviation for three measurements. The central bar represents the mean. Data are presented as mean ± standard deviation.

peak around −0.3 to −0.4 V was noticed during negative scan, with the concurrent emergence of a new diffraction peak at 43.3° in GIXRD pattern, corresponding to the (111) plane of Cu. Following the negative scan, diffraction peaks at 50.5° and 74.1° also appeared, corresponding to the (200) and (220) crystal planes of Cu, respectively. The intensity of these three peaks becomes progressively higher with decreasing potential. Upon further reduction of the potential to −0.8 V, the diffraction peak corresponding to the (101) plane of Zn intensifies, indicating the commencement of Zn deposition. Conversely, the anodic peaks during positive scan correspond to the stripping of Cu and Zn, together with the gradual disappearance of diffraction peaks. The sequential appearance of the Cu and Zn diffraction peaks suggests the earlier nucleation of zincophilic Cu sites, thus enhancing Zn^{2+} adsorption, decreasing the nucleation overpotential of Zn[50], and promoting subsequent homogeneous deposition of dual-metal CuZn layers. This staged nucleation and growth is further investigated by ex situ XPS during plating (−1.0 V, Supplementary Fig. S18). Distinct Zn2*p* and Cu2*p* peaks were observable in the plated metal layer, and peak shift/broadening was also notable with varying deposition times. In the initial stage, the broad half-peak width and the presence of satellite peaks (942.8 eV) of the Cu2$p_{1/2}$ and Cu2$p_{3/2}$ multiplet peaks suggest that Cu primarily exists as Cu^{2+} and Cu^{+} [55,56]. With prolonged deposition time, the half-peak width of the Cu2$p_{1/2}$ and Cu2$p_{3/2}$ split peaks gradually decreases, and the satellite peaks vanish, indicating a transition of Cu species predominantly to metallic Cu^{0} [56]. Concurrently, the relative changes in Cu and Zn content during deposition (Fig. 3b) also demonstrate the preferential nucleation of Cu and subsequent growth of dual-metal CuZn layers.

Further electrochemical impedance spectroscopy (EIS) at different temperatures was utilized to analyze the deposition kinetics and quantify the activation energy of CuZn-RME (Supplementary Fig. S19). Clearly, a smaller charge transfer resistance (R_{ct}) is attained in C1Z5H20 than in both C0Z1H20 and C1Z5, explaining the fast CuZn-RME switching in C1Z5H20. The R_{ct} values at different temperatures were also recorded, where C1Z5H20 electrolyte shows consistently lower values than those of C0Z1H20 and C1Z5 electrolytes (Supplementary Fig. S19). Compared to the deposition of CuZn in C1Z5 (7.6 kJ mol^{-1}) and Zn in C0Z1H20 (10.6 kJ mol^{-1}) electrolytes, the lower activation energy for CuZn deposition in C1Z5H20 (6.7 kJ mol^{-1}) reveals the key role of Cu^{2+} and H^{+} introduction in optimizing the kinetics of reversible CuZn bimetallic electroplating. The lower oxophilicity of Cu and its inherent inertness to HER can effectively prevent the side reactions[50], and H^{+} can accelerate the stripping kinetics of CuZn bimetal and reduce the formation of Cu/Zn oxide/hydroxide compounds, endowing highly reversible CuZn-RME in aqueous electrolyte. Additionally, FTO electrodes plated (Cu and CuZn) in C1Z0H20 and C1Z5H20

electrolytes were exposed to air for one week to assess the anti-oxidation capability of plated metal layers. After one-week of air exposure, plated Cu in C1Z0H20 showed obvious inhomogeneities, and the Cu primarily exists in the form of Cu^{2+} and Cu^{+}, while plated CuZn in C1Z5H20 remained a gray-black appearance and stable oxidation state of Cu^{0} (Supplementary Figs. S20 and S21). This suggests that the plated CuZn layer can effectively suppress Cu oxidation, probably due to the altered local electronic structure and chemical properties of Cu in CuZn dual-metal layers. With the lower activation energy and higher CE (Supplementary Fig. S22), CuZn-RME also shows excellent durability, maintaining $\Delta T > 40\%$ after 3000 cycles (Fig. 3c). Gradually increasing ΔT was notable in the first ~400 cycles, which is likely due to necessary activation steps. The ΔT (~47% at 41st cycle and ~43% at 2998th cycle, Supplementary Fig. S23a) and switching kinetics (t_c 7 s, t_b 4 s at 41st cycle and t_c 7 s, t_b 3 s at 2998th cycle) were stabilized in the following cycles, offering excellent ΔT retention of above 90% (Fig. 3c, Supplementary Fig. S23).

The integration and performance of quasi-solid-state CuZn-RMEDs

Albeit the excellent CE, switching kinetics, and cycling stability achieved in a well-tuned C1Z5H20 aqueous electrolyte, assembly of RMEDs using aqueous electrolyte poses problems of volatility, susceptibility to leakage during prolonged operation, and poor tolerance under extreme conditions[57–59]. In contrast, hydrogel electrolytes, favored for their safety, biocompatibility, and high transparency, feature abundant hydrophilic functional groups on polymer chains that facilitate the ion migration through the gel network, thereby ensuring homogenous ion flux for ECDs[46–48,60,61]. PAM, known for its flexibility, mechanical properties, high transparency, and ionic conductivity[62–64], is thus adopted in our work for the assembly of quasi-solid-state CuZn-RMEDs. Prior to the assembly of RMEDs, the feasibility of hydrogel electrolytes for CuZn-RME was evaluated in three-electrode testing (Supplementary Fig. S24). Apparently, hydrogel C1Z5H20 electrolyte features high transparency (Fig. 4a), with a fast switching kinetics ($t_c = 14.0$ s, $t_b = 4.0$ s) and large ΔT (58%) comparable to aqueous system. Moreover, the hydrogel electrolyte exhibits comparable bulk resistance (Supplementary Fig. S25) and ionic conductivity to aqueous counterpart (11.3 vs. 17.4 mS cm^{-1}), surpassing most reported studies (Supplementary Table S1). Such a high ionic conductivity is conducive to rapid metal ion transport. Subsequently, hydrogel C1Z5H20 electrolyte was employed to assemble quasi-solid-state CuZn-RMED (10×10 cm^2, Fig. 4b), which achieved a decent optical modulation ($\Delta T = 57\%$) at relatively extended switching times ($t_c = 15.0$ s, $t_b = 24.0$ s) (Fig. 4c). Notably, this switching time is slower than those reported in Ag-based RMEs[30,65], which may be attributed to the inherent divalent character, increased ionic radius of Cu^{2+}/Zn^{2+} ions, and the relatively lower ionic conductivity of hydrogel electrolyte, rendering slower interfacial ion transport kinetics and elevated energy barriers for metal ions plating/striping. Nonetheless, the integration of quasi-solid-state hydrogel electrolyte significantly enhanced the bi-stability of CuZn-RMEDs, showing superior memory effect compared to aqueous electrolyte-based counterpart (Fig. 4d), increasing energy efficiency for RMEDs. Calculations of color coordinates in the CIE1931 chromaticity diagram revealed that the tinted CuZn-RMEDs pertain to nearly color neutrality (Supplementary Fig. S26), ensuring a high color rendering index pursued for smart window applications[5]. Meanwhile, the as-developed quasi-solid-state hydrogel electrolytes enable scalable assembly (20×20 cm^2, Supplementary Fig. S27) and customized patterning to meet diverse application scenarios (Fig. 4e, Supplementary Fig. S28). Notably, due to differences in ohmic resistance caused by geometric structures, the current distribution on electrode surfaces is often uneven, leading to voltage decay and varying deposition speeds between edges and centers (Supplementary Fig. S29), especially in large-area devices. Nonetheless, the relatively high ionic conductivity of the hydrogel electrolyte can mitigate the voltage decay effect, ensuring uniform distribution of ionic flux and allowing deep tinting across the RMEDs. Future efforts in mitigating the voltage decay effect involve developing a mesh electrode or embedding bus bars in FTO electrodes, as well as electrolyte engineering[10,53,66].

Additionally, the quasi-solid-state CuZn-RMEDs exhibit excellent broad-band optical modulation capability, realizing a low T% of <6% across the solar spectrum (Fig. 4f). The effective NIR light blocking endowed the CuZn-RMEDs with efficient thermal insulation capabilities, which could be visually represented by the temperature difference in thermal images. When placed on a heating plate (30–70 °C), CuZn-RMEDs in a transparent state only provide a temperature difference of about 2–9 °C (center of the RMEDs vs. heating plate, Supplementary Fig. S30). In contrast, tinted CuZn-RMEDs exhibit superior heat-blocking capability, offering larger temperature differences of 6–14 °C (Fig. 4g).

A wide operating temperature range is crucial for the performance of RMEDs in extreme environments. To assess the temperature adaptability of CuZn-RMEDs, CV and dynamic transmittance measurements at different temperatures (60, 20, 0, and −20 °C) were conducted (Fig. 5a–c, Supplementary Figs. S31 and S32). CuZn-RMEDs with aqueous electrolyte show good electrochemical reversibility and large ΔT at 20 and 60 °C (Fig. 5a, b), but soon degrade at the lowered temperature of 0 and −20 °C (Fig. 5c, Supplementary Figs. S31 and S32). Comparatively, the quasi-solid-state CuZn-RMEDs manifest excellent electrochemical reversibility and large ΔT (~40%) across the 60 to −20 °C range.

To unveil the anti-freezing capability of hydrogel electrolytes, spectroscopic analysis was performed to investigate the bonding information in aqueous and quasi-solid-state hydrogel electrolytes. Fourier transform infrared spectroscopy (FTIR) revealed feature peaks of water molecules and hydrogels (Supplementary Fig. S33). The peak at 1620 cm^{-1} was attributed to the stretching vibration of $-CONH_2-$, and the broad peak at 3300–3700 cm^{-1} was attributed to the stretching vibration of O–H bonds. The spectral shift of the hydrogel electrolyte indicates the restructuring of the hydrogen bond network and enhanced proton capture capability. The O–H stretching vibration of water molecules at 3300–3700 cm^{-1} can be fitted into three components, with the symmetric O–H stretching vibration near 3200 cm^{-1} attributed to the strong O–H…O (strong HBs) interactions, while the asymmetric O–H stretching vibrations observed at 3400 and 3560 cm^{-1} are attributed to medium H-bonds (medium HBs) and weak O–H…O (weak HBs) interactions between adjacent O atoms (polymer–water or water–water)[67,68]. The relatively lower ratio of strong HBs in hydrogel electrolytes (hydrogel 26% vs. aqueous 45%) indicates that polymer segments provide additional hydrogen bond receptor/donor sites and participate in hydrogen bond network restructuring, with strong polymer-water interactions trapping free water molecules. Similarly, Raman spectroscopy (Supplementary Fig. S34) also shows a weakening of the strong HBs peak at 3200–3300 cm^{-1} and a broadening of the medium HBs peak at 3400–3500 cm^{-1}, indicating the formation of dynamic weak hydrogen bonds at the water-amide interface, a transition from strong HBs to polymer-dependent weak HBs, and the disruption of the ordered tetrahedral structure of water molecules. This dynamic regulation of the hydrogen bond network enables the hydrogel to maintain an amorphous water network structure at low temperatures[69]. Differential scanning calorimetry (DSC) test further evidenced the lowered freezing point in hydrogel electrolytes (hydrogel −38 °C vs. aqueous −18 °C, Supplementary Fig. S35), reflecting a lower starting temperature for the freezing phase transition within the hydrogel[70] and explaining its excellent freeze resistance. Such a hydrogel electrolyte has enabled quasi-solid-state CuZn-RMEDs with excellent light modulation capability, near color neutrality, extended memory effect, broader operational

https://doi.org/10.1038/s41467-025-66963-7

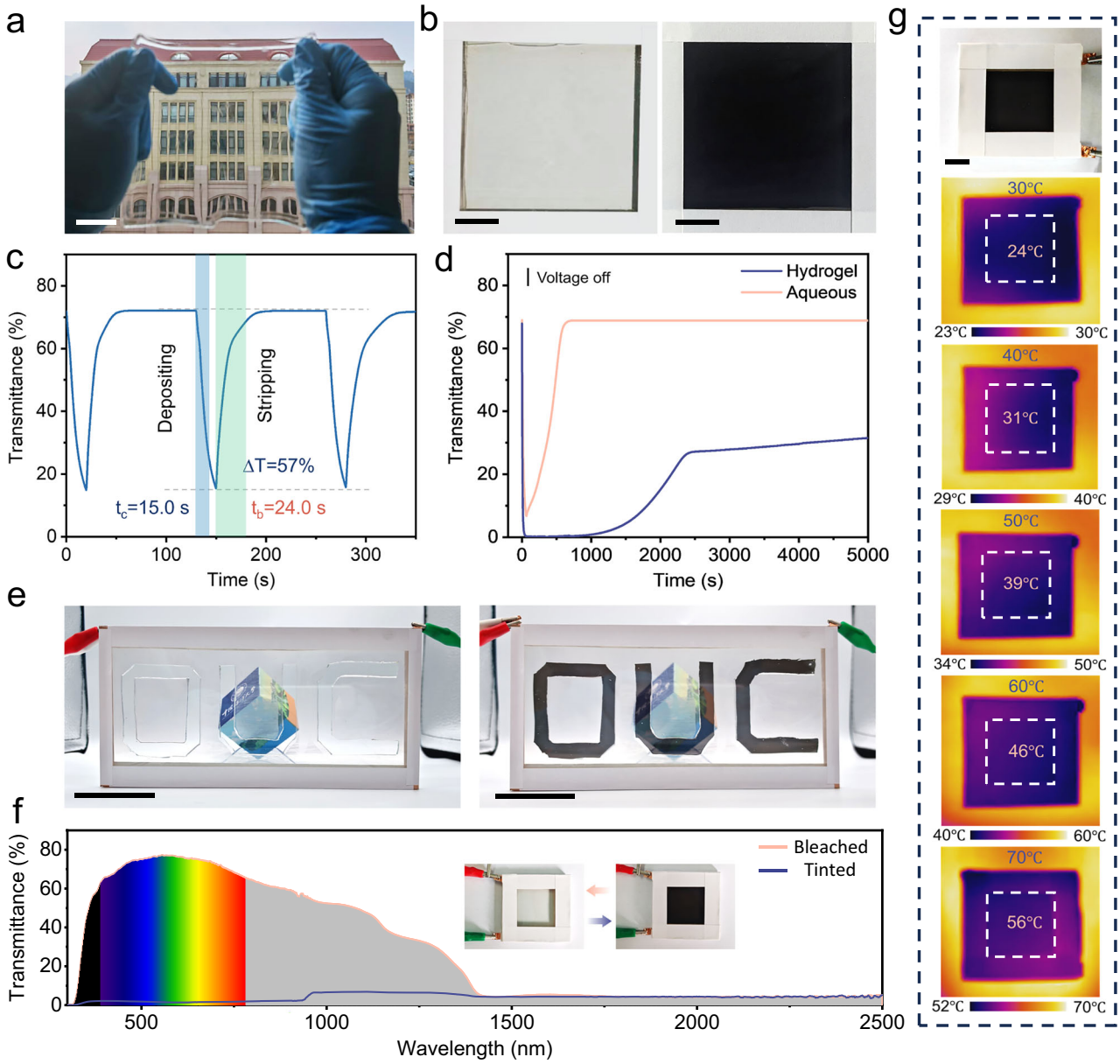

Fig. 4 | Assembly and performance evaluation of quasi-solid-state CuZn reversible metal electrodeposition-based electrochromic devices (CuZn-RMEDs). a Photograph of hydrogel C1Z5H20 (Cu^{2+}/Zn^{2+} ratio of 1:5 with an H^+ concentration of 20 mM) electrolyte, scale bar 2 cm. **b** Photographs of quasi-solid-state CuZn-RMEDs in bleached (left) and tinted (right) states, scale bar 2 cm. **c** Transmittance (@550 nm) of quasi-solid-state CuZn-RMEDs during tinting and bleaching. **d** Memory effect of quasi-solid-state and liquid-state CuZn-RMEDs. **e** Photographs of patternable quasi-solid-state CuZn-RMEDs, scale bar 5 cm. **f** Transmittance spectrum (300–2500 nm) and photographs of quasi-solid-state CuZn-RMEDs in tinted and bleached states. **g** Photograph and thermal images of tinted quasi-solid-state CuZn-RMEDs at different heating temperatures, the active areas of the devices are highlighted by dashed white frames in the thermal images, scale bar 1 cm.

temperature window, and leakage-free properties, meeting the demands of most practical scenarios.

Although the above advances have been achieved, factors including cost-effectiveness (Supplementary Table S2) and environmental impact should still be considered for implementation of RMEDs. Therefore, reusing the transparent electrodes and electrolyte is considered an effective strategy to reduce costs and minimize environmental impact[42]. In this regard, the self-standing hydrogel electrolyte greatly simplified the RMED assembly process, needless of sealant and electrolyte injection steps, making it facile to disassemble the RMEDs to recycle the FTO glass and electrolytes. As such, we attempt to reutilize the FTO glass by performing simple cleaning during its services in quasi-solid-state CuZn-RMEDs (Fig. 5d inset). After every 100 cycles, the device will be disassembled, and the FTO glass and hydrogel electrolyte will be cleaned and reused to reassemble the quasi-solid-state CuZn-RMEDs. It is clearly seen that such a simple cleaning step can not only effectively remove the accumulated by-products (Supplementary Fig. S36) and allow the effective recycling of the costly transparent conductor, but also ensures excellent tinting/bleaching reversibility and optical modulation during extended cycling.

The recycled FTO electrode (cleaning every 100 cycles) retained a stable current response in RMEDs and ΔT of 67% after 500 cycles, while the ΔT of RMED with the untreated FTO electrode soon degraded to 45% after 500 times of continuous cycling (Supplementary Figs. S37 and S38). The effectiveness of FTO recycling is further

https://doi.org/10.1038/s41467-025-66963-7

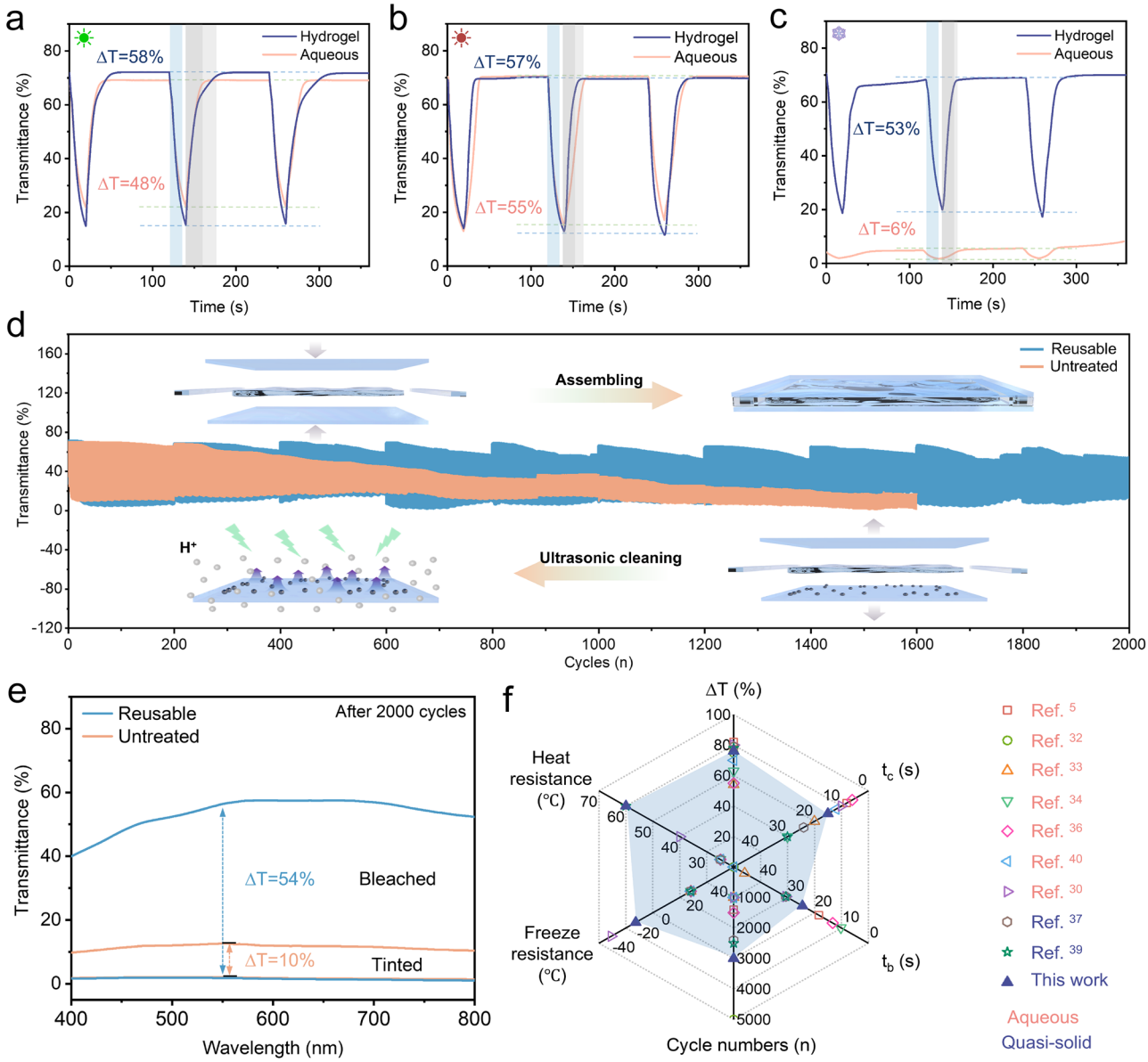

Fig. 5 | Operational temperature range and F-doped SnO_2 (FTO) glass recycling in quasi-solid-state CuZn reversible metal electrodeposition-based electrochromic devices (CuZn-RMEDs). Transmittance versus time curves of quasi-solid-state and aqueous CuZn-RMEDs at **a** 20°C, **b** 60°C, and **c** 0 °C. **d** Transmittance (@550 nm) variation of quasi-solid-state CuZn-RMED in tinted (−1.2 V, 25 s) and bleached (0.8 V, 75 s) states during 2000 cycles for both untreated FTO electrode and reusable FTO electrode (cleaning every 200 cycles), inset is the schematic diagram of the recycling and cleaning process. **e** Transmittance spectrum of CuZn-RMEDs in tinted and bleached states after 2000 cycles. **f** Comparison of this work with other RME-based studies.

validated in 2000 times cycling. With a recycled FTO electrode, RMEDs maintained stable optical switching and current response after 2000 cycles (cleaned every 200 cycles), and still exhibited a large ΔT of 54% (@550 nm) after cleaning (Fig. 5d, e, Supplementary Fig. S39). In contrast, RMED with an untreated FTO electrode showed obvious ΔT degradation and current fluctuations after hundreds of cycles, with ΔT dropping to only 10% (@550 nm) after 2000 cycles. This may be attributed to the prominent accumulation of CuZn bimetallic nanoparticles and the formation of irreversible metal compounds during continuous cycling (Supplementary Fig. S40).

Moreover, similar to FTO recycling, the hydrogel electrolyte also demonstrated recyclability via cleaning and re-soaking in dual-metal C1Z5H20. The recycled hydrogels present excellent visual transparency, well-maintained optical transmittance, and chemical structural stability after 2000 cycles (Supplementary Figs. S41–S43). Benefiting from the unique staged nucleation mechanism of the CuZn layer and the synergistic effect of the hydrogel electrolyte, the quasi-solid-state CuZn RMEDs show superior light and heat modulation capability, enhanced durability, and widened temperature adaptability compared to other works (Fig. 5f, Supplementary Table S3). Additionally, the reusability of RMEDs endows them with distinctive economic viability and environmental sustainability.

Energy saving potential of CuZn-RMEDs

The thermal and optical properties of windows significantly impact the energy consumption of buildings. Quasi-solid-state CuZn-RMEDs with excellent light blocking capability are thus adopted for building energy modulation. A medium-sized office building model equipped with dynamic smart windows was constructed using OpenStudio, and the energy-saving potential of quasi-solid-state CuZn-RMEDs in different climatic conditions was simulated in conjunction with EnergyPlus. While realistic factors such as device degradation, voltage decay, and

https://doi.org/10.1038/s41467-025-66963-7

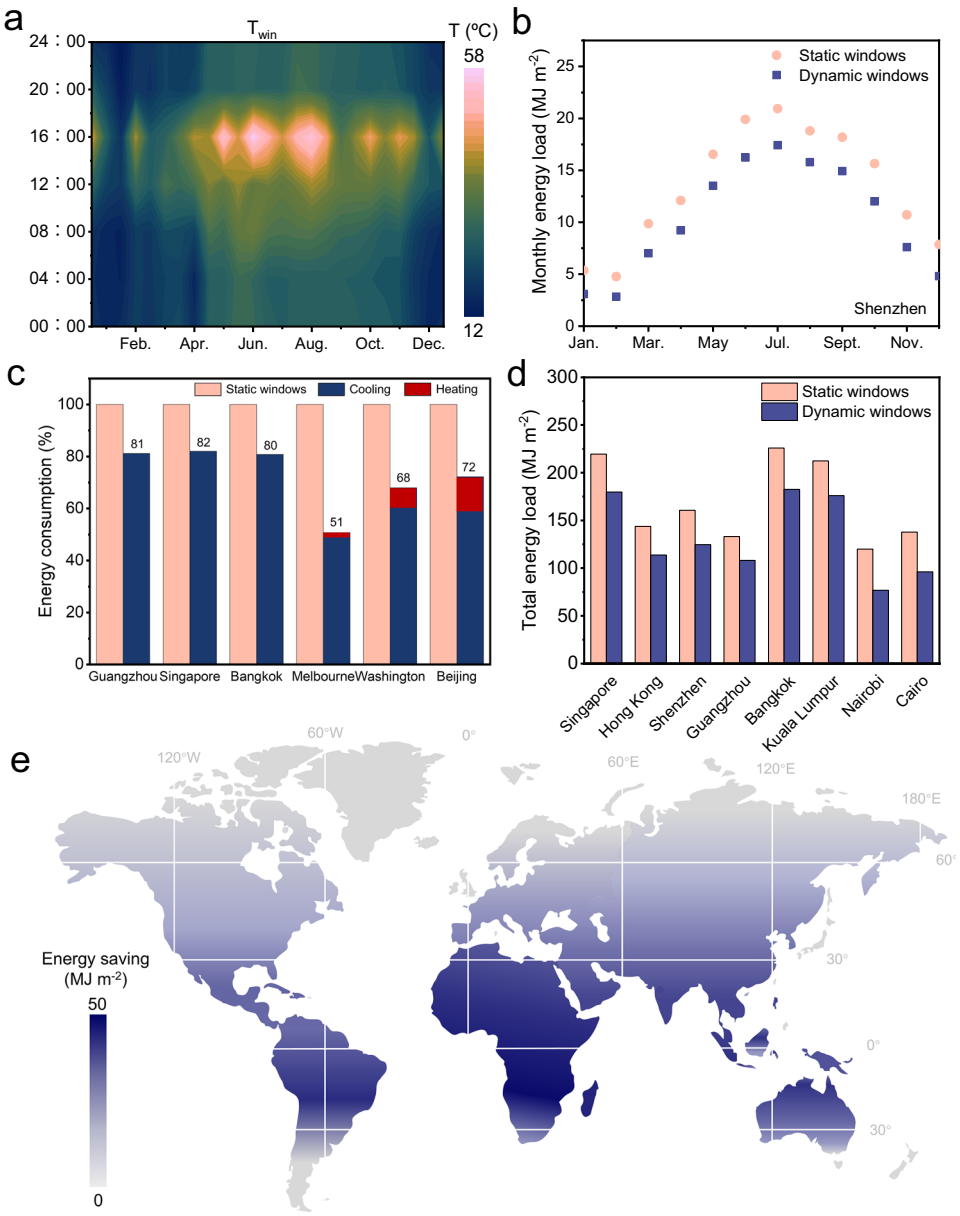

Fig. 6 | Building energy consumption simulation and calculation with quasi-solid-state CuZn reversible metal electrodeposition-based electrochromic devices (CuZn-RMEDs) dynamic windows. a Hourly monthly image of internal surface temperatures of windows in Shenzhen (China). **b** Annual energy loads calculation for dynamic and static windows in Shenzhen. **c** Percentage of cooling and heating energy savings (dynamic vs. static windows) at six different latitudes. **d** Calculation of annual total energy consumption of buildings in eight different regions around the world. **e** Global simulation and evaluation of energy saving performance of quasi-solid-state CuZn-RMED dynamic windows.

temperature-dependent response times can affect the actual energy saving of CuZn-RMEDs, these simulations are still viable to estimate the energy-saving performance achievable with quasi-solid-state RMEDs and represent the theoretical upper limit of their energy-saving potential. Initially, the hourly to monthly inner surface temperature of windows in Shenzhen (China) was calculated based on the weather files in EnergyPlus database (Fig. 6a). It can be seen that in summer, sustained solar insolation can cause the internal surface temperature of windows to reach up to 50 °C, leading to increased indoor temperatures and enhanced air conditioning energy consumption for cooling. After that, the energy saving effect of quasi-solid-state CuZn-RMEDs dynamic windows in one year was analyzed based on the climate data of Shenzhen and the optical performance of CuZn-RMEDs (Supplementary Table S4). As shown in Fig. 6b, dynamic windows achieve a reduction in energy demand for all months and are able to reduce total annual energy consumption by about 22% compared to static windows. Considering that ECWs do not always need to reach dark-tinted states in practice (for example, in winter), we also conducted energy consumption simulations for the intermediate tinting state (defined as dimmed state, Supplementary Table S4 and Fig. S44) to demonstrate the dynamic energy saving capability of CuZn-RMEDs. The results show that even in the dimmed state, ECWs can still notably reduce annual total energy consumption in different cities (Supplementary Fig. S45), for example, ~19% in Shenzhen.

Due to the significant differences in heating and cooling demands across various latitudes, the energy-saving effects of dynamic windows also vary. For low latitudes, where sunlight intensity is high for most of the year, energy consumption is primarily derived from indoor cooling, and the energy-saving effects of dynamic windows are more pronounced (Fig. 6c). The calculated annual total energy demand for

dynamic windows in eight different global regions (Fig. 6d, Supplementary Fig. S45b) revealed that, compared to static windows, dynamic windows can reduce energy consumption by up to 18–33%. Finally, the energy-saving effects of quasi-solid-state CuZn-RMEDs in 20 global cities were calculated, and the global energy-saving performance was also assessed. The results demonstrated that our dynamic CuZn-RMEDs smart windows exhibit excellent energy benefits, especially in tropical regions (Fig. 6e), with the potential to save up to 50 MJ m^{-2} of energy consumption (equivalent to 196 kg m^{-2} of CO_2 emissions).

Discussion

In summary, we formulated dual-metal hydrogel electrolyte to assemble quasi-solid-state CuZn-RMED dynamic windows having excellent broadband optical modulation ($\Delta T\%$ = 78%@550 nm), nearly color neutrality, fast switching kinetics (t_c = 15.0 s, t_b = 24.0 s), wide operational temperature range (−20 to 60 °C), recyclability (2000 cycles) and efficient building energy modulation across different climatic regions, addressing the challenges of limited light blocking capability, short cycling life and cost issues of currently available EC smart windows. The dual-metal electrolyte was optimized with an appropriate amount of Cu^{2+} (Cu^{2+}:Zn^{2+} molar ratio of 1:5) and pH tuning, effectively reducing the activation energy of metal plating (6.7 kJ mol^{-1}), realizing staged nucleation, promoting homogeneous deposition of dual-metal CuZn nanoparticles, and ensuring excellent plating/stripping reversibility (ΔT retention over 90% after 3000 cycles) and fast switching kinetics. Moreover, the formulated PAM-hydrogel electrolyte can provide uniform ion flux, inhibit undesirable side reactions, and disrupt the ordered tetrahedral structure of water molecules, enabling assembly of leakage-free, wide-temperature operable, patternable, scalable, and recyclable quasi-solid-state CuZn-RMEDs. The quasi-solid-state CuZn-RMEDs can reach deeply tinted dark states ($T\%$ < 6% in 300–2500 nm) and exhibit significant energy-saving effects in different regions and climates, with up to a 33% reduction in building energy consumption in tropical regions. This CuZn-RMED dynamic window with simple configuration, wide operating temperature range, broadband regulation, reusability, and energy efficiency has showcased a great leap forward for smart windows. The advantages achieved in this work will be of great interest for future development of energy-efficient and smart optoelectronic devices towards green buildings, sustainability, and decarbonization.

Methods

Materials and preparation of CuZn electrolyte

Zinc (II) sulfate heptahydrate ($ZnSO_4{\cdot}7H_2O$), potassium chloride (KCl), and hydrochloric acid (HCl) were purchased from Sinopharm Chemical. Copper (II) chloride dihydrate ($CuCl_2{\cdot}2H_2O$) was purchased from Aladdin. FTO (F-doped SnO_2) glass was purchased from Wuhan Jingge Solar Technology Co. For the preparation of C1Z5H20 electrolyte, $ZnSO_4{\cdot}7H_2O$ (200 mM), $CuCl_2{\cdot}2H_2O$ (40 mM), KCl (1000 mM), and HCl (20 mM) were dissolved in deionized water and stirred for 1 h at room temperature. CZ electrolytes with different Cu^{2+}:Zn^{2+} ratios and C1Z5H electrolytes with different HCl concentrations were also prepared for comparison. FTO (7 Ω) glass was employed as the transparent conducting electrode in all electrochemical studies and device fabrication.

Preparation of hydrogel CZH electrolyte

Acrylamide (AM), potassium persulfate ($K_2S_2O_8$), and N,N-methylene-bis (acrylamide) (MBA) were purchased from Aladdin. For the preparation of polyacrylamide (PAM) hydrogels, AM (4225 mM), $K_2S_2O_8$ (3 mM), and MBA (3 mM) were dissolved sequentially in deionized water and stirred for 1 h to obtain the precursor solution, which was then transferred to a closed mold and heated at 60°C for 3 h to obtain PAM hydrogels. After that, the PAM hydrogel was saturated in the C1Z5H20 electrolyte obtained above for 24 h to obtain the hydrogel CZH electrolyte.

Assembly process of quasi-solid-state CuZn-RMEDs

Quasi-solid-state CuZn-RMEDs employed FTO glass as the working electrode, Ag wires adhered to FTO glass as the counter electrode, with hydrogel C1Z5H20 electrolyte encapsulated in between. To ensure uniform electrical contact, copper foil was placed along the perimeter of FTO electrodes. The hydrogel C1Z5H20 electrolyte was then placed between the working and counter electrode, and the device was sealed with epoxy adhesives. The size of the CuZn-RMEDs can reach 10 cm × 10 cm with an effective area of about 9 cm × 9 cm.

Material characterizations

The microstructure and topography of the deposited metal films were observed by scanning electron microscopy (Gemini SEM 300). The phase composition and surface chemical properties of the plated metal layers on FTO electrodes were characterized by powder Grazing Incidence X-ray diffraction (GIXRD, Bruker D8) and X-ray photoelectron spectroscopy (XPS, Thermo Scientific K-Alpha). Raman spectroscopy was performed by a laser Raman spectrometer (HORIBA LabRAM HR800, laser excitation: 532 nm). Fourier Transform infrared (FTIR) spectroscopy was performed by a Fourier Transform Infrared spectrometer (Thermo Fisher Scientific Nicolet iS20). Differential scanning calorimetry was performed by a differential scanning calorimeter (HITACHI DSC200) in N_2 atmosphere. The samples were first cooled at a rate of 10 °C min^{-1} to −60 °C and then heated to 20 °C. The pH of the electrolytes was measured by the Leici PHS-3E pH meter. Thermal images were captured using the Fluke TiX640 Infrared Camera.

Electrochemical characterizations

Electrochemical tests were performed on an electrochemical workstation (CHI760E, Shanghai Chenhua Instruments, Inc.). Cyclic voltammetry (CV) scans and multi-potential steps were conducted using a three-electrode system with a Pt sheet as the counter electrode, Ag/AgCl as the reference electrode, and FTO as the working electrode. Electrochemical impedance spectroscopy (EIS) measurements were performed in the frequency range of 0.01–100 kHz. UV–Vis spectrophotometer (UV-2600i, Shimadzu) was used for in-situ and ex-situ optical performance tests.

Calculation of ionic conductivity of electrolytes

The intrinsic ionic conductivity σ (S cm^{-1}) of electrolytes can be calculated by the following equation (Eq. (1)):

$$\sigma = \frac{d}{R_e \times S} \tag{1}$$

d is the thickness of the measured sample (cm). R_e is the intrinsic impedance of the measured sample (Ω), which can be obtained from the electrochemical impedance spectroscopy Nyquist plots. S is the effective area of the electrode (cm^2).

Energy-saving performance simulation

To evaluate the impact of CuZn-RMEDs as smart windows on heating/cooling loads of the building, we constructed a model of a medium-sized office building equipped with dynamic smart windows using OpenStudio and simulated the energy-saving effect coupled with EnergyPlus. The dimensions of the building are 20 m × 20 m × 3 m, and the windows are 2 m × 10 m in size and evenly distributed on the four walls. The energy efficiency of the building was demonstrated by comparing the heating/cooling loads required when applying the quasi-solid-state CuZn RMED dynamic smart windows or the normal static windows. To maintain comfort in the office area, the system

considers that when the room temperature is above 22 °C, the windows are switched to a tinted state, and the cooling mode is turned on. When the room temperature is lower than 22 °C, the windows are switched to the bleached state and open the heating mode. In addition, in order to more accurately reflect the actual energy saving effect of smart windows, the simulation process refers to the General Code for Energy Efficiency and Renewable Energy Application in Buildings (GB55015), which comprehensively takes into account the building's air conditioning and heating system running time, circulation of office persons, and the impact of lighting equipment on the building's energy consumption. The parameters required for the energy consumption simulation were calculated from the actual measured spectral data (Supplementary Table S4). The specific parameters can be calculated by the following equation (Eqs. (2)–(5)):

$$T_{\mathrm{vis/sol}} = \frac{\int I_{\mathrm{vis/sol}} T(\lambda)\mathrm{d}\lambda}{\int I_{\mathrm{vis/sol}}\mathrm{d}\lambda} \tag{2}$$

$T_{\mathrm{vis/sol}}$ is the solar transmittance at wavelength of 380–780 nm/300–2500 nm, $T(\lambda)$ is the spectral transmittance (380–780 nm for T_{vis} and 300–2500 nm for T_{sol}). $I_{\mathrm{vis/sol}}$ is the standard luminous efficiency function of photopic vision for the wavelength of 380–780 nm and solar irradiance spectra for AM1.5 G, respectively.

$$T_{inf} = \frac{\int I_{inf} T(\lambda)\mathrm{d}\lambda}{\int I_{inf}\mathrm{d}\lambda} \tag{3}$$

T_{inf} is the solar transmittance (1500–2500 nm). I_{inf} is the solar irradiance spectra for AM1.5 G at a wavelength of 1500–2500 nm. $T(\lambda)$ is the spectral transmittance (1500–2500 nm).

$$R_{\mathrm{vis/sol}} = \frac{\int I_{\mathrm{vis/sol}} R(\lambda)\mathrm{d}\lambda}{\int I_{\mathrm{vis/sol}}\mathrm{d}\lambda} \tag{4}$$

$R_{\mathrm{vis/sol}}$ is the solar reflectance at wavelength of 380–780 nm/300–2500 nm, $R(\lambda)$ is the spectral reflectance (380–780 nm for R_{vis} and 300–2500 nm for R_{sol}).

$$R_{inf} = \frac{\int I_{inf} R(\lambda)\mathrm{d}\lambda}{\int I_{inf}\mathrm{d}\lambda} \tag{5}$$

R_{inf} is the solar reflectance (1500–2500 nm). I_{inf} is the solar irradiance spectra for AM1.5 G at a wavelength of 1500–2500 nm. $R(\lambda)$ is the spectral reflectance (1500–2500 nm).

According to Kirchhoff's law, the spectral emissivity ($\varepsilon_{\mathrm{inf}}$) is equal to the spectral absorption (α_{inf}). Since the smart window is essentially opaque in the infrared-band, its spectral emissivity in the inf-band can be obtained by $\varepsilon_{\mathrm{inf}} = \alpha_{\mathrm{inf}} = 1 - R_{\mathrm{inf}}$, considering the low T% in this wavelength range.

Calculation of total annual heating and cooling energy consumption for office buildings should be in accordance with the following provisions:

The total annual heating and cooling energy consumption E (kWh m^{-2}) should be calculated according to the following equation (Eq. (6)):

$$E = E_{\mathrm{H}} + E_{\mathrm{C}} \tag{6}$$

E_{H} is the annual heating consumption (kWh m^{-2}). E_{C} is the annual cooling power consumption (kWh m^{-2}).

The annual heating energy consumption of buildings in hot summer and warm winter areas, hot summer and cold winter, and mild areas should be calculated according to the following equation (Eq. (7)):

$$E_{\mathrm{H}} = \frac{Q_{\mathrm{H}}}{A \times COP_{\mathrm{H}}} \tag{7}$$

Q_{H} is the cumulative annual heat consumption (kWh), which is calculated by dynamic simulation software. A is the total floor area (m^2). $\mathrm{COP_H}$ is the comprehensive performance coefficient of the heating system, taking 2.6.

The annual cooling consumption should be calculated according to the following equation (Eq. (8)):

$$E_{\mathrm{C}} = \frac{Q_{\mathrm{C}}}{A \times \mathrm{COP_C}} \tag{8}$$

Q_{C} is the cumulative annual cooling consumption (kWh), which is calculated by dynamic simulation software. A is the total building area (m^2). $\mathrm{COP_C}$ is the comprehensive performance coefficient of the cooling system of public buildings, taking 3.5; for residential buildings in cold regions, hot summer and cold winter, hot summer and warm winter regions, taking 3.6.

The actual energy saving should be calculated according to the following equation (Eq. (9)):

$$E_{\mathrm{A}} = E_{\mathrm{G}} - E_{\mathrm{i}} \tag{9}$$

E_{A} is the actual energy savings, E_{G} is the gross energy savings generated by the RMEDs intervention, E_{i} is the energy consumed by the operation of the RMEDs itself.

Based on weather files from the EnergyPlus database, we simulated the energy consumption of buildings in 20 cities around the world, including Singapore, Hong Kong, Shenzhen, Guangzhou, Bangkok, Kuala Lumpur, Nairobi, Cairo, Beijing, Haikou, Mumbai, Harare, Rio, Manila, Washington, Mexico City, Quito, Sydney, Melbourne, and Sao Paulo.

Reporting summary

Further information on research design is available in the Nature Portfolio Reporting Summary linked to this article.

Data availability

All relevant data, Supplementary Figs. and calculations supporting the study's conclusions are available within this paper and its supplementary information, or may be obtained upon request from the corresponding author. Source data are provided with this paper.

References

1. Korgel, B. A. Composite for smarter windows. *Nature* **500**, 278–279 (2013).
2. Goldstein, E. A., Raman, A. P. & Fan, S. Sub-ambient non-evaporative fluid cooling with the sky. *Nat. Energy* **2**, 17143 (2017).
3. Transparent aerogels reduce energy loss through building windows. *Nat. Energy* **8**, 327–328 (2023).
4. Zhao, F. et al. Inorganic electrochromic smart windows for advancing building energy efficiency. *Nat. Rev. Clean. Technol.* **1**, 396–412 (2025).
5. Zhang, Y. et al. Color-neutral smart window enabled by gradient reversible alloy deposition. *ACS Energy Lett.* **9**, 4162–4171 (2024).
6. Xu, B. et al. The progress and outlook of multivalent-ion-based electrochromism. *Small Sci.* **3**, 2300025 (2023).
7. Li, H., Zhang, W. & Elezzabi, A. Y. Transparent zinc-mesh electrodes for solar-charging electrochromic windows. *Adv. Mater.* **32**, 2003574 (2020).
8. Li, T. et al. A radiative cooling structural material. *Science* **364**, 760–763 (2019).

9. Wang, K. et al. Thermo-responsive poly(N-isopropylacrylamide)/hydroxypropylmethyl cellulose hydrogel with high luminous transmittance and solar modulation for smart windows. *ACS Appl. Mater. Interfaces* **15**, 4385–4397 (2023).
10. Chen, J. et al. The birth of zinc anode-based electrochromic devices. *Appl. Phys. Rev.* **11**, 011316 (2024).
11. Meng, W. et al. Photochromic thermoelectric smart window for season-adaptive solar heat and daylight management. *Adv. Funct. Mater.* **34**, 2402494 (2024).
12. Feng, W. et al. Achieving controllable thermochromic fluorescence via synergistic intramolecular charge transfer and molecular packing. *Angew. Chem. Int. Ed.* **64**, e202415815 (2024).
13. Ke, Y. et al. Smart Windows: electro-, thermo-, mechano-, photochromics, and beyond. *Adv. Energy Mater.* **9**, 1902066 (2019).
14. Yang, G. et al. Advances in nanomaterials for electrochromic devices. *Chem. Soc. Rev.* **49**, 8687–8720 (2020).
15. Zydlewski, B. Z. & Milliron, D. J. Dual-band electrochromic devices utilizing niobium oxide nanocrystals. *ACS Appl. Mater. Interfaces* **16**, 24920–24928 (2024).
16. Zhang, S., Cao, S., Zhang, T. & Lee, J. Y. Plasmonic oxygen-deficient TiO_2-nanocrystals for dual-band electrochromic smart windows with efficient energy recycling. *Adv. Mater.* **32**, 2004686 (2020).
17. Zhang, S., Cao, S., Zhang, T., Fisher, A. & Lee, J. Y. Al^{3+} intercalation/de-intercalation-enabled dual-band electrochromic smart windows with a high optical modulation, quick response and long cycle life. *Energy Environ. Sci.* **11**, 2884–2892 (2018).
18. Huang, Z. et al. An efficient and flexible bifunctional dual-band electrochromic device integrating with energy storage. *Nano-Micro Lett.* **17**, 98 (2024).
19. Liu, R., Li, Y., Hu, B. & Long, Y. Organic ligand-free scalable dual-band electrochromic smart windows. *Adv. Funct. Mater.* **35**, 2409914 (2025).
20. Shao, Z. et al. Tri-band electrochromic smart window for energy savings in buildings. *Nat. Sustain.* **7**, 796–803 (2024).
21. Raman, A. P., Anoma, M. A., Zhu, L., Rephaeli, E. & Fan, S. Passive radiative cooling below ambient air temperature under direct sunlight. *Nature* **515**, 540–544 (2014).
22. Zhai, Y. et al. Scalable-manufactured randomized glass–polymer hybrid metamaterial for daytime radiative cooling. *Science* **355**, 1062–1066 (2017).
23. Lu, N. et al. Electric-field control of tri-state phase transformation with a selective dual-ion switch. *Nature* **546**, 124–128 (2017).
24. Bhoumik, N. C. et al. Nonaqueous electrolytes for reversible zinc electrodeposition for dynamic windows with excellent optical contrast and durability. *Joule* **8**, 1036–1049 (2024).
25. Zhou, Y., Zhang, X., Ding, Y., Zhang, L. & Yu, G. Reversible deposition of lithium particles enabled by ultraconformal and stretchable graphene film for lithium metal batteries. *Adv. Mater.* **32**, 2005763 (2020).
26. Sheng, S.-Z. et al. Nanowire-based smart windows combining electro- and thermochromics for dynamic regulation of solar radiation. *Nat. Commun.* **14**, 3231 (2023).
27. Wang, S. et al. Scalable thermochromic smart windows with passive radiative cooling regulation. *Science* **374**, 1501–1504 (2021).
28. Li, J. Y., Juarez-Rolon, J. S., Islam, S. M. & Barile, C. J. Electrolyte effects in reversible metal electrodeposition for optically switching thin films. *J. Electrochem. Soc.* **166**, D496 (2019).
29. Zhou, J. & Han, Y. Design of a widely adjustable electrochromic device based on the reversible metal electrodeposition of Ag nanocylinders. *Nano Res.* **16**, 1421–1429 (2023).
30. Zhang, J. et al. Aprotic polar electrolyte facilitates indoor dynamic optical-thermal management in silver-based electro-reflective smart windows. *J. Phys. Chem. C* **128**, 5768–5776 (2024).
31. Eh, A. L.-S., Lin, M.-F., Cui, M., Cai, G. & Lee, P. S. A copper-based reversible electrochemical mirror device with switchability between transparent, blue, and mirror states. *J. Mater. Chem. C* **5**, 6547–6554 (2017).
32. Eh, A. L.-S., Chen, J., Zhou, X., Ciou, J.-H. & Lee, P. S. Robust trioptical-state electrochromic energy storage device enabled by reversible metal electrodeposition. *ACS Energy Lett.* **6**, 4328–4335 (2021).
33. Wang, L., Jiao, X., Chen, D. & Wang, T. A solar water-heating smart window by integration of the water flow system and the electrochromic window based on reversible metal electrodeposition. *Adv. Sci.* **9**, 2104121 (2022).
34. Hernandez, T. S. et al. Bistable black electrochromic windows based on the reversible metal electrodeposition of Bi and Cu. *ACS Energy Lett.* **3**, 104–111 (2018).
35. Li, J. Y. & Barile, C. J. Reversible electrodeposition of Ni and Cu for dynamic windows. *J. Electrochem. Soc.* **168**, 092501 (2021).
36. Guo, X. et al. Heat-insulating black electrochromic device enabled by reversible nickel–copper electrodeposition. *ACS Appl. Mater. Interfaces* **14**, 20237–20246 (2022).
37. Eh, A. L.-S. et al. A quasi-solid-state tristate reversible electrochemical mirror device with enhanced stability. *Adv. Sci.* **7**, 1903198 (2020).
38. Zhang, W. et al. Highly reversible zinc metal anode in a dilute aqueous electrolyte enabled by a pH buffer additive. *Angew. Chem. Int. Ed.* **62**, e202212695 (2023).
39. Islam, S. M. & Barile, C. J. Dynamic windows using reversible zinc electrodeposition in neutral electrolytes with high opacity and excellent resting stability. *Adv. Energy Mater.* **11**, 2100417 (2021).
40. Madu, D. C. et al. Investigating formate, sulfate, and halide anions in reversible zinc electrodeposition dynamic windows. *ACS Appl. Mater. Interfaces* **14**, 47810–47821 (2022).
41. Lee, G. H. et al. Recent advances in reversible metal electrodeposition-based smart windows. *Electron. Mater. Lett.* **20**, 657–683 (2024).
42. Wang, Y. et al. Sustainable, low-cost, high-contrast electrochromic displays via host–guest interactions. *Proc. Natl. Acad. Sci. USA* **121**, e2401060121 (2024).
43. Li, W., Dahn, J. R. & Wainwright, D. S. Rechargeable lithium batteries with aqueous electrolytes. *Science* **264**, 1115–1118 (1994).
44. Wang, F. et al. Stabilizing high voltage $LiCoO_2$ cathode in aqueous electrolyte with interphase-forming additive. *Energy Environ. Sci.* **9**, 3666–3673 (2016).
45. Wang, F. et al. Hybrid aqueous/non-aqueous electrolyte for safe and high-energy Li-ion batteries. *Joule* **2**, 927–937 (2018).
46. Wang, Y. et al. Lean-water hydrogel electrolyte for zinc ion batteries. *Nat. Commun.* **14**, 3890 (2023).
47. Ai, X. et al. Zinc polyacrylamide hydrogel electrolyte for quasi-solid-state electrochromic devices with low-temperature tolerance. *Cell Rep. Phys. Sci.* **3**, 101148 (2022).
48. Hina, M., Bashir, S., Kamran, K., Ramesh, S. & Ramesh, K. Synthesis and characterization of self-healable poly (acrylamide) hydrogel electrolytes and their application in fabrication of aqueous supercapacitors. *Polymer* **210**, 123020 (2020).
49. Qi, R. et al. Gel polymer electrolyte toward large-scale application of aqueous zinc batteries. *Adv. Funct. Mater.* **33**, 2306052 (2023).
50. Zhou, L. et al. Zincophilic Cu sites induce dendrite-free Zn anodes for robust alkaline/neutral aqueous batteries. *Adv. Funct. Mater.* **32**, 2110829 (2022).
51. Geng, L. et al. Organic-solvent-free primary solvation shell for low-temperature aqueous zinc batteries. *Chem* **11**, 102302 (2024).
52. Chen, X. et al. A thin and homogeneous solid electrolyte interface enriched with ZnF_2 and ZnS for highly reversible zinc batteries. *Energy Storage Mater.* **75**, 103984 (2025).
53. Strand, M. T. et al. Polymer inhibitors enable >900 cm^2 dynamic windows based on reversible metal electrodeposition with high solar modulation. *Nat. Energy* **6**, 546–554 (2021).

54. Hernandez, T. S. et al. Electrolyte for improved durability of dynamic windows based on reversible metal electrodeposition. *Joule* **4**, 1501–1513 (2020).
55. Cheng, T. Q., Griffiths, K., Norton, P. R. & Puddephatt, R. J. XPS studies of copper deposition from 1,5-cyclooctadiene–copper(I)–hexafluoroacetylacetonate on Si(111). *Appl. Surf. Sci.* **126**, 303–308 (1998).
56. Avila, J. R. et al. Atomic layer deposition of Cu(i) oxide films using Cu(ii) bis(dimethylamino-2-propoxide) and water. *Dalton Trans.* **46**, 5790–5795 (2017).
57. Tsao, C.-H., Su, H.-M., Huang, H.-T., Kuo, P.-L. & Teng, H. Immobilized cation functional gel polymer electrolytes with high lithium transference number for lithium ion batteries. *J. Membr. Sci.* **572**, 382–389 (2019).
58. Tao, L. et al. Highly improved photocurrent and stability of dye-sensitized solar cell through quasi-solid-state electrolyte formed by two low molecular mass organogelators. *Org. Electron.* **65**, 179–184 (2019).
59. Cai, H., Chen, Z., Guo, S., Ma, D. & Wang, J. Polyacrylamide gel electrolyte for high-performance quasi-solid-state electrochromic devices. *Sol. Energy Mater. Sol. Cells* **256**, 112310 (2023).
60. Virya, A. & Lian, K. Lithium polyacrylate–polyacrylamide blend as polymer electrolytes for solid-state electrochemical capacitors. *Electrochem. Commun.* **97**, 77–81 (2018).
61. Silvaraj, D. S. et al. Tailorable solid-state supercapacitors based on poly (N-hydroxymethylacrylamide) hydrogel electrolytes with high ionic conductivity. *J. Energy Storage* **35**, 102320 (2021).
62. Gao, D., Lv, J. & Lee, P. S. Natural polymer in soft electronics: opportunities, challenges, and future prospects. *Adv. Mater.* **34**, 2105020 (2022).
63. Kim, J. W. et al. Self-healing strain-responsive electrochromic display based on a multiple crosslinked network hydrogel. *Chem. Eng. J.* **430**, 132685 (2022).
64. Kim, J. et al. Stretchable, self-healable, and photodegradable supercapacitor based on a polyelectrolyte crosslinked via dynamic host–guest interaction. *Chem. Eng. J.* **422**, 130121 (2021).
65. Zhang, S., Cao, S., Zhang, T. & Lee, J. Y. Plasmonic oxygen-deficient TiO_{2-x} nanocrystals for dual-band electrochromic smart windows with efficient energy recycling. *Adv. Mater.* **32**, 2004686 (2020).
66. Li, H., Firby, C. J. & Elezzabi, A. Y. Rechargeable aqueous hybrid Zn^{2+}/Al^{3+} electrochromic batteries. *Joule* **3**, 2268–2278 (2019).
67. Zhang, Q. et al. Modulating electrolyte structure for ultralow temperature aqueous zinc batteries. *Nat. Commun.* **11**, 4463 (2020).
68. Zhu, B. et al. Accelerated proton transport modulates dynamic hydrogen bonding networks in eutectic gel electrolytes for low-temperature aqueous Zn-metal batteries. *J. Energy Chem.* **109**, 325–336 (2025).
69. Feng, D., Jiao, Y. & Wu, P. Proton-reservoir hydrogel electrolyte for long-term cycling Zn/PANI batteries in wide temperature range. *Angew. Chem. Int. Ed.* **62**, e202215060 (2023).
70. Li, Q. et al. A wide-temperature adaptive electrochromic device based on a poly(vinyl alcohol)/poly(acrylic acid) gel electrolyte. *Adv. Funct. Mater.* **35**, 2415874 (2025).

Acknowledgements

This work was financially supported by the National Natural Science Foundation of China (No. 52572186 and 52202320 to J.C.), Shandong Excellent Young Scientists Fund Program (Overseas, Grant No. 2023HWYQ-060 to J.C.), and the Fundamental Research Funds for the Central Universities (Grant Nos. 202201013153 and 202401032131 to J.C.).

Author contributions

B.X. and J.C. conceived the idea and initiated the experimental design. B.X. W.W. Y.Z. (Yingxin Zhang), and C.Q. carried out the device fabrication, electrochemical experiments, and characterizations. B.X. wrote the paper. B.X., Y.Z. (Yingxin Zhang), C.Q., Y.Z. (Yue Zhu), J.W., W.T., M.H., H.W., P.S.L., and J.C. reviewed, discussed, and edited the manuscript. J.C. supervised the project.

Competing interests

The authors declare no competing interests.

Additional information

Supplementary information The online version contains supplementary material available at https://doi.org/10.1038/s41467-025-66963-7.

Correspondence and requests for materials should be addressed to Huanlei Wang, Pooi See Lee or Jingwei Chen.

Peer review information *Nature Communications* thanks Hongli Sun, Ashutosh K. Singh, and the other, anonymous, reviewer(s) for their contribution to the peer review of this work. A peer review file is available.

Reprints and permissions information is available at http://www.nature.com/reprints

Publisher's note Springer Nature remains neutral with regard to jurisdictional claims in published maps and institutional affiliations.

Open Access This article is licensed under a Creative Commons Attribution-NonCommercial-NoDerivatives 4.0 International License, which permits any non-commercial use, sharing, distribution and reproduction in any medium or format, as long as you give appropriate credit to the original author(s) and the source, provide a link to the Creative Commons licence, and indicate if you modified the licensed material. You do not have permission under this licence to share adapted material derived from this article or parts of it. The images or other third party material in this article are included in the article's Creative Commons licence, unless indicated otherwise in a credit line to the material. If material is not included in the article's Creative Commons licence and your intended use is not permitted by statutory regulation or exceeds the permitted use, you will need to obtain permission directly from the copyright holder. To view a copy of this licence, visit http://creativecommons.org/licenses/by-nc-nd/4.0/.

© The Author(s) 2025